# On the Detection Capabilities of Underwater Distributed Acoustic Sensing

Itzhak Lior, Anthony Sladen, Diane Rivet, Jean-Paul Ampuero, Yann Hello, Carlos Becerril, Hugo F. Martins, Patrick Lamare, Camille Jestin, Stavroula Tsagkli, et al.

## HAL Id: hal-03229358
## https://hal.science/hal-03229358v2

Submitted on 29 Nov 2021

1    # On the Detection Capabilities of Underwater DAS
2
3    Itzhak Lior[1], Anthony Sladen[1], Diane Rivet[1], Jean-Paul Ampuero[1], Yann Hello[1],
4    Patrick Lamare[2], Camille Jestin[3], Stavroula tsagkli[4] and Christos Markou[4].

5
6    [1]Université Côte d'Azur, CNRS, Observatoire de la Côte d'Azur, IRD, Géoazur

7    [2]Aix Marseille Université, CNRS/IN2P3, CPPM

8    [3]Febus-optics, Pau, France

9    [4]NCSR Demokritos, Institute of Nuclear and Particle Physics, Ag. Paraskevi
10   Attikis, Athens, Greece

11
12   Corresponding author: Itzhak Lior (itzhaklior22@gmail.com)

13

## Key Points:

15   ● The noise content of underwater DAS along three different
16   telecommunication cables is quantified and compared to adjacent
17   broadband stations.

18   ● Earthquake detection capabilities using DAS are similar to those of
19   broadband instruments.

20   ● Detection capabilities are mainly a function of the recorded noise, cable
21   response and apparent velocity.

**Abstract**

22

23   The novel technique of distributed acoustic sensing (DAS) holds great
24   potential for underwater seismology by transforming standard
25   telecommunication cables, such as those currently traversing most of the
26   world's oceans, into dense arrays of seismo-acoustic sensors. To harness
27   these measurements for seismic monitoring, the ability to record transient
28   ground deformations using telecommunication fibers is investigated here by
29   analyzing ambient noise, earthquake signals, and their associated phase
30   velocities, on DAS records from three dark fibers in the Mediterranean Sea.
31   The recording quality varies dramatically along the fibers and is strongly
32   correlated with the bathymetry and the apparent phase velocities of the
33   recorded waves. Apparent velocities are determined for several well-
34   recorded earthquakes and used to convert DAS S-wave strain spectra to
35   ground motion spectra. Excellent agreement is found between the spectra of
36   nearby underwater and on-land seismometers and DAS converted spectra,
37   when the latter are corrected for site effects. Apparent velocities greatly
38   affect the ability to detect seismic deformations: for the same ground
39   motions, slower waves induce higher strains and thus are more favorably
40   detected than fast waves. The effect of apparent velocity on the ability to
41   detect seismic phases, quantified by expected signal-to-noise ratios, is
42   investigated by comparing signal amplitudes predicted by an earthquake
43   ground motion model to recorded noise levels. DAS detection capabilities on
44   underwater fibers are found to be similar to those of nearby broadband
45   sensors, and superior to those of on-land fiber segments. The results
46   demonstrate the great potential of underwater DAS for seismic monitoring
47   and earthquake early warning.

**1 Introduction**

48

49   To date, most observational earthquake research relies on ground
50   motions recorded by seismometers. These instruments are typically installed
51   in proximity to active faults, as the most valuable observations are those
52   obtained very close to earthquake epicenters: they provide the most
53   coherent view of source processes and allow for early detection of large
54   earthquakes and monitoring of small ones. However, there is a severe
55   observational gap: the vast majority of seismometers are located on-land,
56   while the largest  earthquakes, and most tsunami generating earthquakes,
57   occur underwater. Existing technologies to overcome this observational gap,
58   e.g., ocean-bottom seismometers (OBS), are very costly and thus not widely
59   implemented. The lacking ocean-bottom monitoring hinders the ability to
60   conduct underwater seismological research. This is especially critical for
61   hazard mitigation tasks such as providing earthquake early warning (EEW)
62   (e.g., Allen and Melgar, 2019; Lior and Ziv, 2020; Vallée et al., 2017) for
63   underwater earthquakes, since precious time is lost waiting for seismic
64   signals to reach on-land stations. Filling this underwater observational gap

65 will greatly benefit hazard mitigation capabilities and constitute a major step
66 forward in seismological research.

67      In recent years, the innovative approach of distributed acoustic
68 sensing (DAS) is being used for many seismological tasks (Zhan, 2019, and
69 reference therein). DAS enables the measurement of transient ground
70 deformations along standard optical fibers such as those inside the
71 telecommunication cables currently traversing most of the world's oceans.
72 Implementing DAS technology on available underwater fibers has great
73 potential to fill the underwater observational gap. The ability to record and
74 analyze earthquakes using underwater DAS has been recently demonstrated
75 (Sladen et al., 2019; Lindsey et al., 2019; Williams et al., 2019), but is yet to
76 be fully realized. To reliably harness this technique for earthquake
77 monitoring, the nature of underwater DAS measurements needs to be better
78 understood.

79      In a previous study, Sladen et al. (2019) used an underwater optical
80 fiber offshore Toulon, South of France, and showed that uneven cable-ground
81 coupling and water-Earth interactions significantly affect the sensitivity to
82 ground motions thus limiting the reliability of earthquake monitoring on
83 underwater telecommunication fibers. Because these underwater cables
84 were installed for the sole purpose of power and data transmission between
85 two points in space, the mechanical coupling between the cable and the
86 ocean-bottom is not uniform along the fiber. This reduces the cable's
87 recording quality to a point that the coupling of several cable segments is
88 insufficient for seismic measurements. The studies by Lindsey et al. (2019)
89 and Willams et al. (2019) relied on seafloor buried cables, which reduced
90 many of these problems, but buried cables are just a small fraction of the
91 global network of seafloor cables. Sladen et al. (2019) also found that
92 underwater DAS earthquake recordings are dominated by Scholte-waves,
93 indicating that acoustic and seismic waves are converted and scattered at
94 the ocean - solid-earth interface. Moreover, interactions between the water-
95 column and solid-earth generate several noise sources, i.e., gravity waves
96 and microseisms, which constitute coherent noise that could affect
97 earthquake monitoring with underwater DAS measurements.

98      Fully unlocking the potential of underwater DAS will facilitate the use of
99 optical fibers as next-generation dense seismic networks, overcoming the
100 disadvantages of discrete, mainly on-land, seismic sensors, thus filling a vast
101 observational gap. A significant first step, is to understand and quantify
102 earthquake detection and measurement abilities and set detection
103 thresholds by characterizing measured noise, seismic signals, and their
104 relation to ground motions. To this end, underwater DAS noise and seismic
105 signals are analyzed here using data recorded by three different underwater
106 DAS fibers, one in France and two in Greece. DAS records are then compared
107 to those of nearby broadband stations, two of which are located underwater.

108    This manuscript is organized as follows. In the next section, the
109  dataset used for this study is described. Then, underwater DAS noise is
110  characterized by computing noise power spectral densities (PSDs). In section
111  4, several cataloged earthquakes are used to analyze the response of the
112  different fibers to ground deformation and the conversion from DAS recorded
113  strain to ground motions. Finally, implications for DAS detection capabilities
114  are discussed.

## 2 Data

116    This study uses an extensive dataset of underwater DAS records,
117  acquired by Géoazur, from three underwater cables: two offshore Methoni,
118  south-west Greece, and one offshore Toulon, South of France. In addition,
119  data from 4 on-land and 2 underwater broadband stations, installed near the
120  cables, are used. The cables' locations, depth profiles, and broadband station
121  locations are shown in Figure 1. Because these cables were simply deployed
122  to provide communication between the two ends of the fiber, the cables'
123  exact geographical position and bathymetric profiles are not well constrained.
124  All cables recorded several local earthquakes during the measurement
125  campaigns; those analyzed in the next sections are indicated in Figure 1 and
126  listed in Table 1. Here, the cables and instrumental setup are described.

127    DAS data from Greece were acquired on two adjacent dark optical
128  fibers, situated on the Central Hellenic Shear Zone, near a triple junction: the
129  Kephalonia Transform Fault to the north-west, and the Hellenic Trench and
130  Mediterranean Ridge to the south-east (Finetti, 1982). These cables are
131  intended for the HCMR (Hellenic Centre for Marine Research) and NESTOR
132  (Neutrino Extended Submarine Telescope with Oceanographic Research)
133  (Aggouras et al., 2005; Anassontzis and Koske, 2003) projects. DAS data
134  were acquired on April 18th and 19th 2019 on the HCMR cable and from April
135  19th to 25th on the NESTOR cable. The HCMR and NESTOR cables span 13.2
136  and 26.2 km, respectively: from a common landing point, they traverse the
137  shallow Methoni bay and then diverge in different directions towards the
138  bottom of the East Ionian Sea (Figure 1). These cables were interrogated
139  using an old generation Febus A1 DAS interrogator, developed by Febus
140  Optics. The gauge length and spatial sampling were set to 19.2 meters for

| Cable name | Origin time | Magnitude | Location (latitude, longitude, depth[km]) | catalog |
|---|---|---|---|---|
| NESTOR | 22/04/2019 19:26:06 | 3.3 | 37.4185, 20.6897, 11.0 | Athens University |
|  | 23/04/2019 17:29:40 | 3.6 | 37.7753, 20.7658, 7.0 | Athens University |
|  | 21/04/2019 22:11:47 | 2.0 | 36.8335, 22.0382, 2.0 | Athens University |
|  | 23/04/2019 19:25:51 | 2.6 | 37.2528, 21.4593, 9.0 | Athens University |
| HCMR | 18/04/2019 21:44:42 | 3.7 | 37.57, 20.66, 8.0 | EMSC |
|  | 19/04/2019 03:30:19 | 2.6 | 37.1523, 20.6662, 1.0 | Athens University |
| MEUST | 19/07/2019 21:16:57 | 2.6 | 44.374, 6.913, 2.6 | Géoazur |
|  | 21/07/2019 23:01:58 | 2.4 | 42.516, 5.143, 2.0 | Géoazur |

Table 1: earthquakes used in this study.

4

141  both cables, equivalent to 688 and 1365 channels of strain-rate equally
142  spaced along the HCMR and NESTOR cables, respectively. Strain-rate was
143  sampled at intervals of 6 milliseconds for HCMR and 5 milliseconds for
144  NESTOR, producing 68 GB and 740 GB of data for HCMR and NESTOR,
145  respectively. In addition to DAS data, several broadband seismometers were
146  available during these DAS measurements: two on-land, deployed near the
147  interrogator for the duration of the measurements, and one permanent OBS
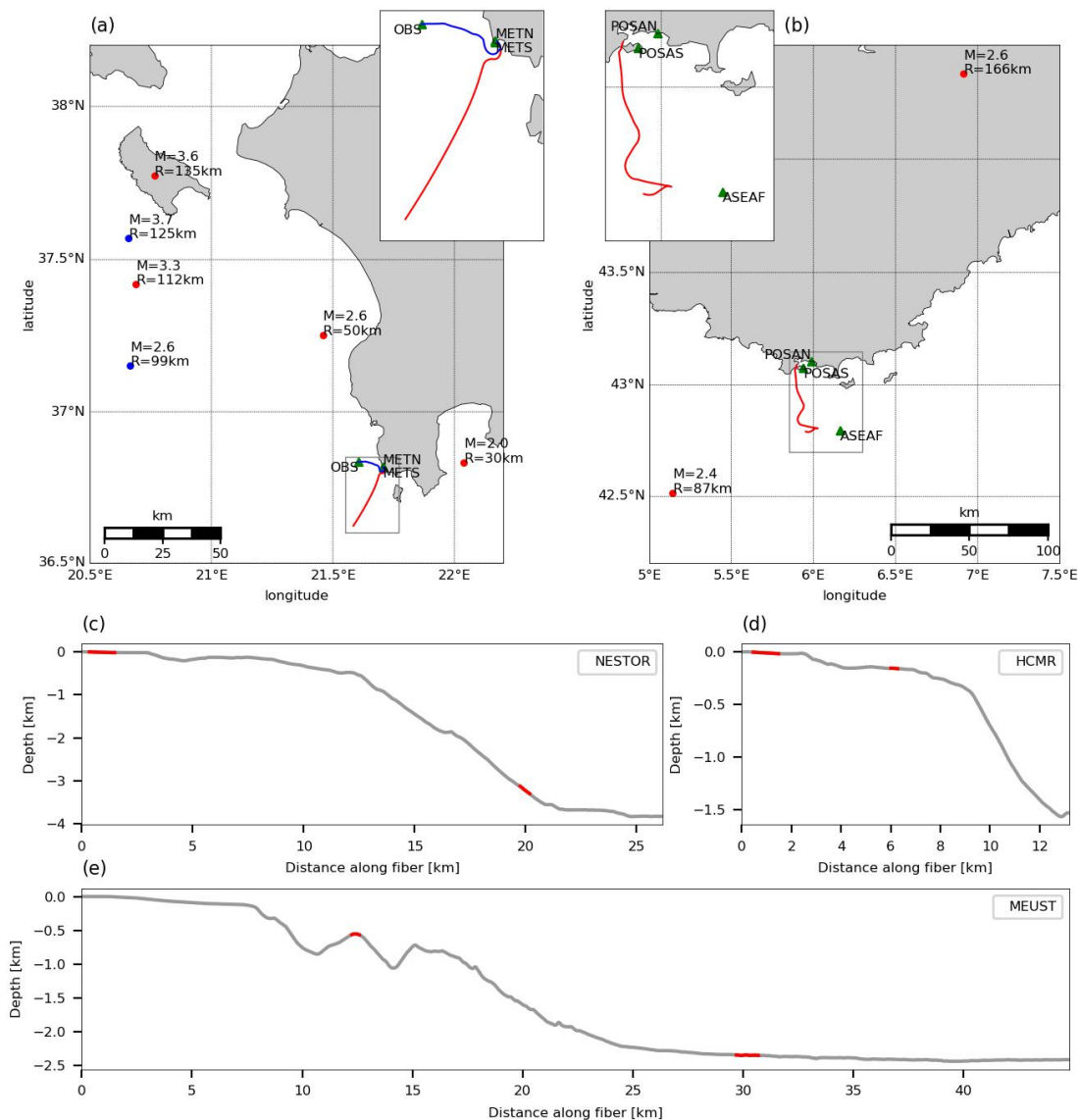


Figure 1: Maps of Methoni and Toulon regions along with cable depth profiles. map of the a) Methoni and b) Toulon regions along with cable locations, broadband stations and analyzed earthquakes. The HCMR, NESTOR and MEUST cables, along with their recorded earthquakes, are indicated in red and blue (left panel), and red (right panel), respectively. Insets correspond to regions marked by gray rectangles. Cable depth profiles are shown in panels (c-e). Sections used in subsequent analysis are indicated in red.

148 near the end of the HCMR cable. Calibration information for the latter, a
149 Guralp CMG40T, was unavailable. The flat frequency response of this sensor,
150 between 30 seconds and 50 Hz, includes the recorded seismic signals, thus,
151 a simple empirical response was estimated by comparing available
152 earthquake records between the OBS and the on-land sensors.

153     The offshore Toulon data were acquired on the same fiber used by
154 Sladen et al. (2019), between July 11th and 31st 2019. The path of this fiber
155 was slightly modified in October 2018, after a first DAS acquisition done by
156 Sladen et al. (2019) (Figure 1). This cable is located in an area of moderate
157 seismicity and is used for the MEUST-NUMerEnv project (Mediterranean
158 Eurocentre for Underwater Sciences and Technologies - Neutrino Mer
159 Environnement) (Lamare, 2016). The cable spans 44.8 km: from the coast to
160 the deep Mediterranean plain. For this cable, an hDAS interrogator (High-
161 Fidelity Distributed Acoustic Sensor), developed by Aragon Photonics, was
162 used, which produces strain measurements. The gauge length and spatial
163 sampling were set to 10 meters, equivalent to 4480 equally spaced channels
164 of strain measured along the cable. Sampling intervals were set to 10 and 2
165 milliseconds for the first and last 10 days of the campaign, respectively,
166 producing 16 TB of data. In addition, 2 on-land broadband sensors, installed
167 near the interrogator, were used. The OBS near the end of the fiber (ASEAF
168 station) was inactive during this measurement campaign, but OBS records
169 from July 2017 were used for noise analysis. These were obtained at a similar
170 time of year, and represent equivalent water temperature (23-24 $^\circ$C) and
171 wave height conditions, as obtained from the Coriolis database
172 (coriolis.eu.org).

### 173 3 DAS Noise Analysis

174     The recorded DAS noise arises from several natural sources, including
175 ocean-solid earth interactions, which produce gravity waves and microseisms.
176 The natural noise amplitude can be affected by local seismic amplification
177 effects. In addition, ground-cable coupling variations modulate the recorded
178 noise and signals, and instrumental noise dominates several frequency-
179 bands along the fibers. In this section, underwater DAS noise is analyzed and
180 quantified.

181     The noise content of underwater DAS records and broadband sensors
182 is quantified by computing PSDs. These PSDs were calculated for the full
183 duration of each campaign at every measurement point along the fibers,
184 following the procedure described in McNamara and Buland (2004). PSDs for
185 the OBS at the end of the HCMR cable were not computed due to missing
186 instrumental response. Because seismic noise PSDs are typically obtained for
187 ground motion accelerations (McNamara and Buland, 2004), here they are
188 calculated for strain-rate; the transition between acceleration and strain-rate,
189 though not straightforward (section 4.2), facilitates a comparison between
190 both measures. While HCMR and NESTOR records were acquired in strain-
191 rate, MEUST strain records were differentiated to strain-rate in the

192  frequency-domain. The PSDs, averaged per measurement location along the
193  fiber, are plotted in Figure *2* as functions of frequency and distance from the
194  interrogator along the fiber. PSDs for selected locations along the cables, as
195  well as for the broadband sensors, are plotted in Figure *3*. The various noise
196  sources shown in Figures *2* and *3* are further described.

197      Solid-earth - ocean-bottom interactions generate several noise sources,
198  recorded by the fibers. At shallow water depths, DAS records are dominated
199  by surface gravity waves at frequencies of 0.05 to 0.3 Hz (black curves in
200  Figure *2* and panels a and c of Figure *3*). The dominant frequency of these
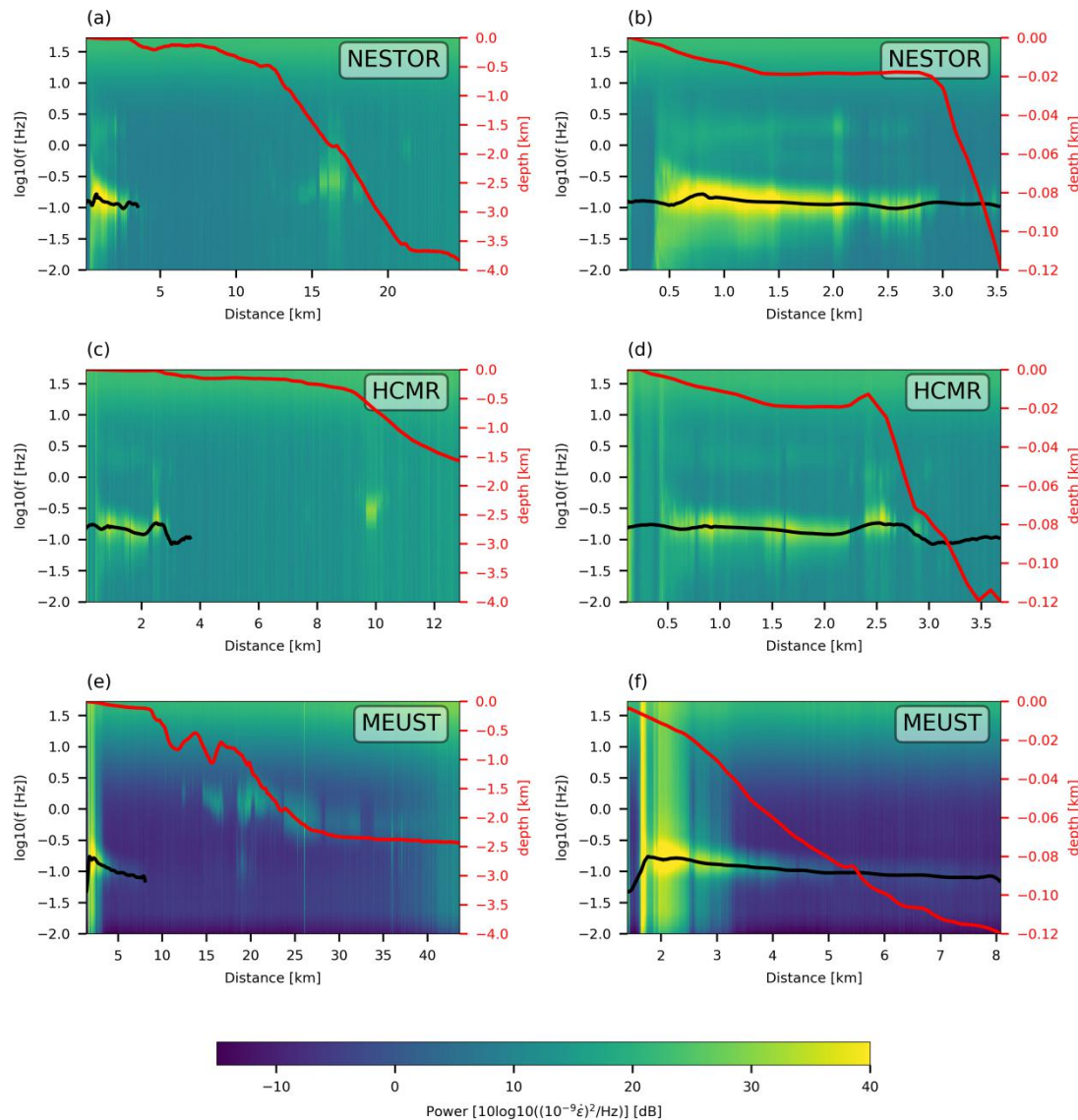


Figure 2: Noise analysis for the 3 cables: average nano-strain-rate PSD as a function of frequency and distance along the fibers. Left panels show the full cable and right panels show the cable up to a water depth of 120 m. Red line indicates bathymetric profiles (right axis), and black lines indicate the peak frequency of gravity waves (frequency associated with the maximum PSD).

201  waves decreases with increasing water depth (red curves in Figure *2*) as
202  predicted by the dispersion relation of surface gravity waves. This effect is
203  also seen in the comparison of HCMR and NESTOR PSDs at 1 and 2km depths
204  (Figure *3*a). Surface gravity wave amplitudes are in close agreement for
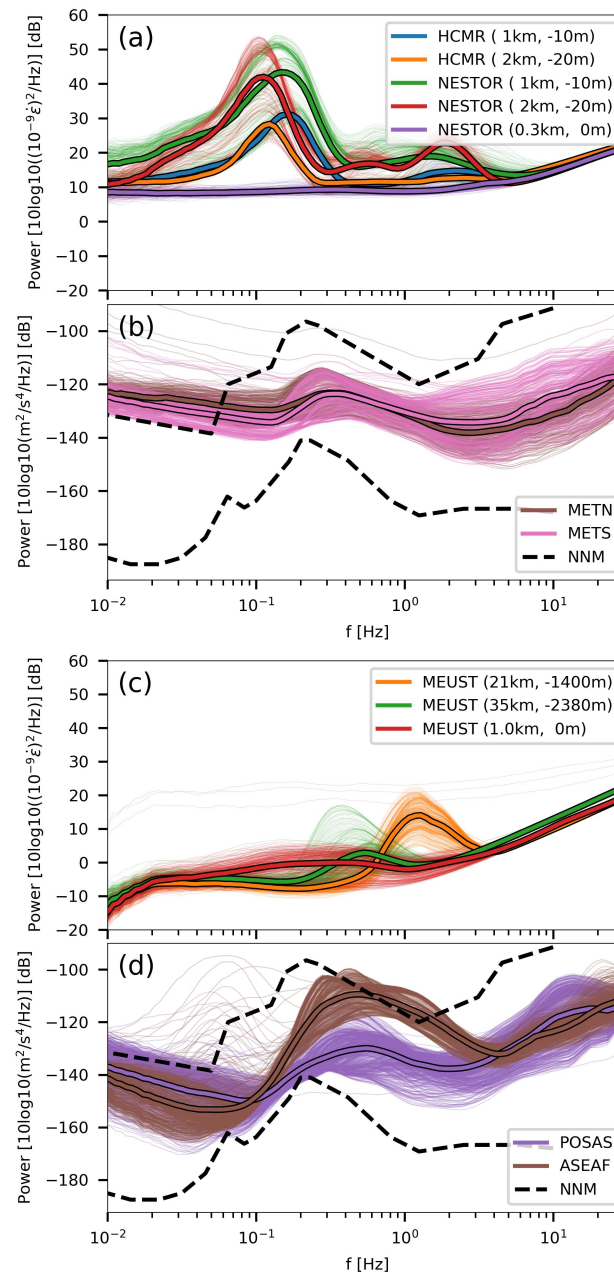


Figure 3: Comparison of DAS (panels a and c) and broadband (panels b and d) PSD. DAS PSDs are displayed for specific distances from the interrogator and water depths as indicated in the panel legends. NESTOR PSD at 0.3 km and MEUST PSD at 1 km correspond to on-land cable segments. Thin and thick lines represent one hour PSD and an average of all available one hour PSDs. The new low and high noise models (Peterson, 1993) are indicated in dashed black lines for broadband data (panels b and d).

205 NESTOR and MEUST in-spite of the different regions and interrogators
206 (panels b and f of Figure *2* and panels a and c of Figure *3*), while those
207 recorded by HCMR are slightly lower. The disparity between gravity wave
208 amplitudes obtained by NESTOR and HCMR, both recorded in Methoni bay,
209 indicate that they are affected by local meteorological conditions: during the
210 NESTOR measurements a storm occurred, inducing higher amplitude gravity
211 waves.

212 HCMR and NESTOR exhibit an additional signature at frequencies of 1
213 to 2 Hz. This signal is a local effect, only observed on cable sections inside
214 Methoni bay, and thus likely related to the seismic response of a
215 sedimentary basin. Full analysis of this signal is beyond the scope of this
216 manuscript, yet its effect on earthquake ground deformations is further
217 described in section *5*.

218 Short fiber stretches are deployed on-land between the DAS
219 interrogators' locations and the shorelines. These extra lengths of fiber
220 provide an opportunity to compare the characteristic noise levels on-land
221 and underwater. The PSDs for NESTOR and MEUST, shown in Figure *3* (panels
222 a and c), indicate lower noise levels than those of underwater segments.
223 However, these short on-land segments, do not record any seismic signals,
224 as further discussed in section *5*.

225 At deeper sections, typically deeper than 2000 meters, the MEUST
226 cable records secondary microseisms, as previously observed by Sladen et al.
227 (2019). These microseisms appear at frequencies of 0.3 to 3 Hz and are the
228 result of interference between ocean waves traveling in opposite directions
229 (Longuet-Higgins, 1950). Similar to gravity waves, secondary microseisms
230 exhibit a frequency decrease with increasing water depth as shown in Figure
231 *2*e and *3*c. The peak frequency recorded at the end of the MEUST cable
232 (green curve in Figure *3*c) matches that observed by the nearby ASEAF OBS
233 (purple curve in Figure *3*d).

234 In addition to natural noise sources, instrumental effects are apparent
235 in Figures *2* and *3*. In several frequency bands and distances along the fibers,
236 instrument (interrogator and fiber) related noise dominates the PSDs
237 (Figures *2* and *3*). These are slightly higher for the old generation
238 interrogator (used in HCMR and NESTOR) than for the new generation one
239 (used in MEUST), and higher for high frequencies than low frequencies
240 (Fernández-Ruiz et al., 2019). Noise levels have spatial fluctuations along the
241 fibers that are persistent in time and similar for different frequencies, as
242 demonstrated in Figure *S1*, where average PSDs are plotted for a section of
243 MEUST. Even though the amplitude and distance scales of the fluctuations
244 could be consistent with those observed for fading (e.g., Gabai and Eyal,
245 2016; Martins et al., 2013), it is not plausible that fading patterns persist for
246 more than several seconds (analyzed PSDs are averaged over many hours).
247 These small fluctuations (typically less than 2 dB) may be a result of the
248 fibers' backscattering pattern, which is known to affect high-frequency noise

249 in chirped-pulse interrogators (Costa et al., 2019), yet further research is
250 needed to understand it over a broader frequency band and for other
251 interrogator types.

252   Since the used cables were deployed over seldom irregular bathymetry
253 (Figure *1*), their ocean-bottom - cable coupling is nonuniform along the
254 cables. This results in gaps in the measurements of coherent signals: gravity
255 waves, microseism signals (Figure *2*), and earthquakes (section *4*). In
256 addition, several fiber segments display oscillating patterns, as seen in
257 Figure *2* (e.g., between 12 and 17 km for NESTOR in panel a), which may be
258 related to the fibers' layout, e.g., high tension segments, cables hanging
259 over seafloor valleys. These patterns will require additional research,
260 possibly involving direct inspections of the cable for validation.

261   Finally, broadband seismometers' noise (panels b and d of Figure *3*)
262 are mostly within the limits of the new low/high noise models (NLNM and
263 NHNM) of Peterson (1993). Expected exceptions are the slightly higher low
264 frequency noise, resulting from the proximity of the stations to the
265 Mediterranean basin (e.g., De Caro et al., 2014), and the high amplitude
266 second microseism peak observed for the ASEAF OBS.

267   The described natural and instrumental noise sources affect
268 earthquake detection and analysis abilities as detailed in following sections.
269 Next, underwater DAS earthquake signals are analyzed and their interactions
270 with observed noise are discussed.

## 4 DAS Earthquake Signals

272   Here, the ability to record earthquakes by underwater DAS, and the
273 response of the different cables to transient ground motions are investigated.
274 Then, apparent velocities are inferred and strain-rate measurements are
275 converted to ground motion accelerations and compared with records of
276 adjacent broadband sensors. To this end, several cataloged earthquakes are
277 analyzed: 2 earthquakes recorded by HCMR, 4 earthquakes recorded by
278 NESTOR, and 2 earthquakes recorded by MEUST. Earthquake locations and
279 magnitudes were taken from one of the available catalogs: European-
280 Mediterranean Seismological Centre (EMSC), University of Athens, or
281 Géoazur catalogs. The earthquake data is summarized in Table *1* and
282 locations, magnitudes and distances to the interrogators appear in Figure *1*.

283   4.1 Cable Response

284   The response of underwater telecommunication fibers to transient
285 deformations is non-uniform; recorded earthquake signals vary in amplitude

10

286  and frequency content along the cable. This is clearly seen in Figure *4* for a
287  magnitude 3.7 earthquake recorded on the HCMR cable (equivalent
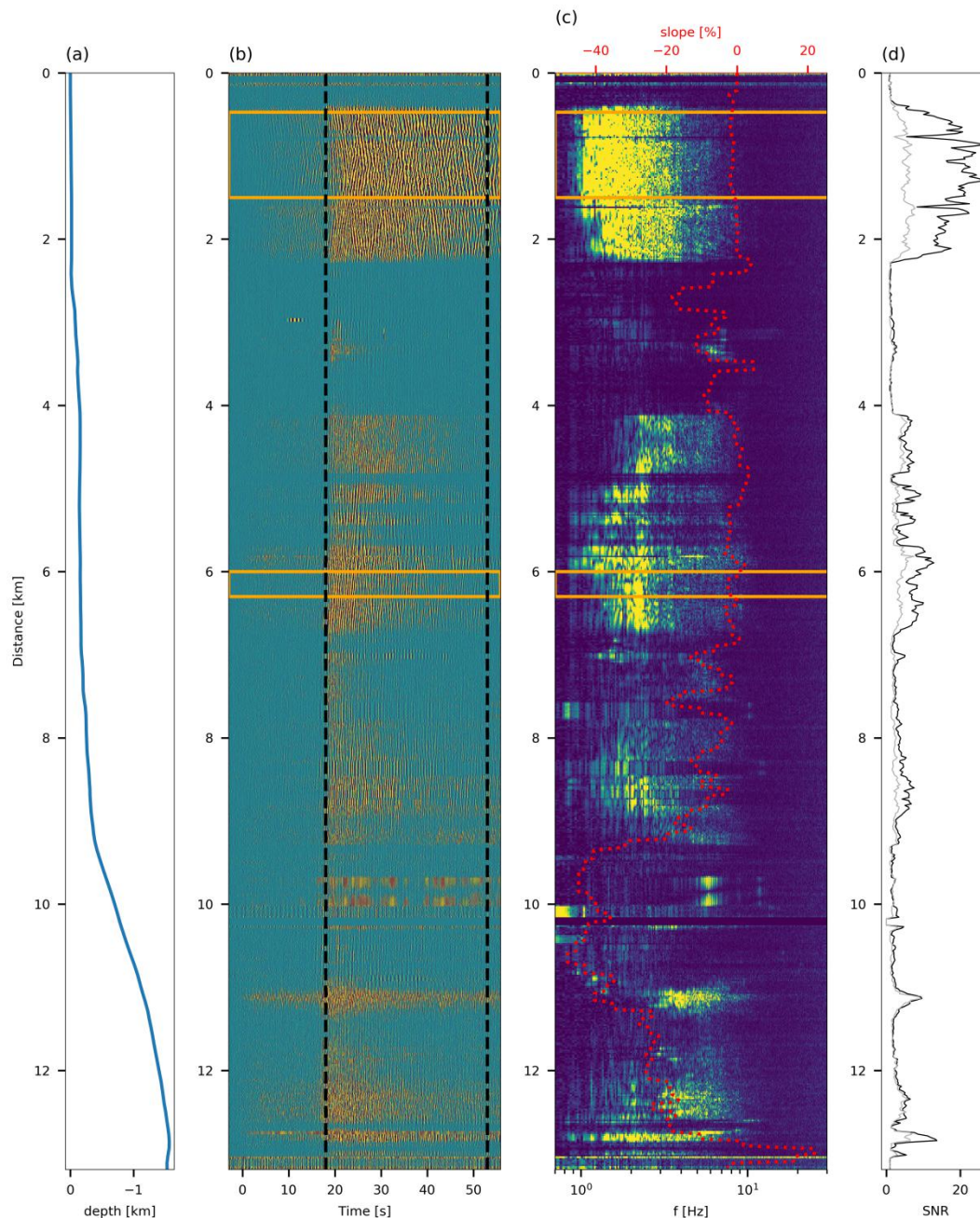288  examples for the NESTOR and MEUST cables are shown in Figures *S2* and *S3*,



Figure 4: Example of a M3.7 earthquake at approximately 125 km recorded by HCMR. a) depth profile, b) earthquake signals, c) spectra and d) signal to noise ratios along the cable's path. Time in panel b is relative to the theoretical P-wave arrival at the cable position of 0 km (closest point to the earthquake epicenter). S-wave spectra in (c) are computed in the interval indicated by dashed black lines in (b). The slope of the cable is plotted in red in panel c. Sections that are used in subsequent analysis are indicted by orange rectangles.

289 respectively). The cable's depth profile (panel a), earthquake time series
290 (panels b), spectra (panels c) and signal-to-noise-ratio (SNR) (Panels d) are
291 plotted as a function of distance along the fiber. These signals are extremely
292 segmented and exhibit amplitude and frequency shifts and jumps (e.g., 5 to
293 6 km). While several cable segments record high amplitude seismic signals,
294 others exhibit very weak amplitudes (e.g., 2.5 to 4 km), or lack seismic
295 signals as seen by the onshore cable segment (0 to 400 meters). SNR were
296 calculated in the frequency-domain by considering signal and noise
297 (obtained in section *3*) amplitudes between 1 and 15 Hz. In panel d, SNR are
298 plotted for the displayed earthquake (black curve) and the other analyzed
299 event on the HCMR cable (gray curve). The similarity between SNR patterns
300 along the fiber for different earthquakes (also seen in Figures *S2* and *S3*)
301 indicates that this cable specific property may be used to quantify ground-
302 cable coupling as well as ground deformation amplifications along the cable.

303 Sections where signals are weak typically correspond to irregular
304 bathymetry, while high amplitude seismic deformations are measured by
305 fiber segments deployed on flat or smooth bathymetry. The latter may be
306 due to the presence of sediments which control amplification and slowness,
307 while the former, may suggest uneven coupling and/or lack of sediments.
308 This correlation is evident when comparing the recorded signals' quality with
309 the bathymetry (Figure *4*a) and slope (red dotted curve in Figure *4*c) along
310 the cable. For example, shallow sections of HCMR and NESTOR record high-
311 energy signals (Figures *4* and *S2*): these segments are deployed inside
312 Methoni bay, a sedimentary basin characterized by flat bathymetry and low
313 velocities (section 4.2). The smooth SNR increase and decrease when
314 entering and exiting the bay (Figures *4*d and *S2*d) suggests the presence of a
315 sedimentary basin: as sediment thickness increases from the edges towards
316 the middle of the basin, so does ground motion amplification. This SNR
317 pattern is thus indicative of cable segments traversing sedimentary basins.

318 In-spite of the often unfavorable ocean-bottom - cable coupling,
319 several cable segments record sufficiently uniform signals for seismic
320 analysis and specifically, apparent velocity estimation. Two such sections are
321 identified for each cable, indicated by orange lines in panels b and c of
322 Figures *4*, *S2* and *S3*. Their signals are analyzed in the following sections.

323 4.2 Strain-rate to ground motions conversion

324 To further investigate the response of underwater DAS to transient
325 ground deformations, DAS signals are compared to the ground motion
326 measurements recorded by nearby seismometers. To convert strain-rate
327 records to ground motions, phase velocities need to be determined. Here, we
328 use the waves' apparent phase velocities along the fiber, assuming the
329 signal is dominated by a single plane wave:

$$\dot{\epsilon}_{xx} = \frac{\partial U_x}{\partial t \partial x} = \frac{\partial V_x}{\partial x} = \frac{\partial V_x}{\partial t}\frac{\partial t}{\partial x} = A_x\frac{1}{C_x}, \tag{1}$$

330  where $\dot{e}_{xx}$, $U_x$, $V_x$, $A_x$ and $C_x$ are the strain-rate, ground displacements,
331  ground velocities, ground accelerations, and apparent phase velocity along
332  the fiber ($x$ direction), respectively. The relation between the phase velocity
333  $C$ and the apparent phase velocity is: $C_x = C/cos\theta$, where $\theta$ is the angle
334  between the wave's propagation direction and the fiber. The apparent
335  velocity is expected to change along the cable due to local conditions,
336  sedimentary cover, seismic wave velocities and propagation direction with
337  respect to the cable's orientation. Here, apparent velocities are estimated
338  via frequency-wavenumber (f-k) analysis, and DAS strain-rate measurements
339  are converted to ground accelerations in the frequency-domain. DAS
340  converted spectra are then compared to broadband seismometer spectra.

341  Apparent velocities are reliably estimated using homogeneous DAS
342  signals recorded on sufficiently long cable segments. Phase apparent
343  velocities are defined as $f/\nu$ where $f$ and $\nu$ are the temporal and spatial
344  frequencies, respectively. This analysis is performed on the segments
345  identified in the previous section (orange lines in panels b and c of Figure *4*,
346  *S2* and *S3*). Example f-k plots are shown in Figure *5* (top panels) for four
347  earthquakes recorded on the NESTOR cable between 0.35 and 1.5 km from
348  the interrogator, on a section deployed in Methoni bay. Similar f-k plots for
349  all cable segments are shown in Figures *S4-S8*.

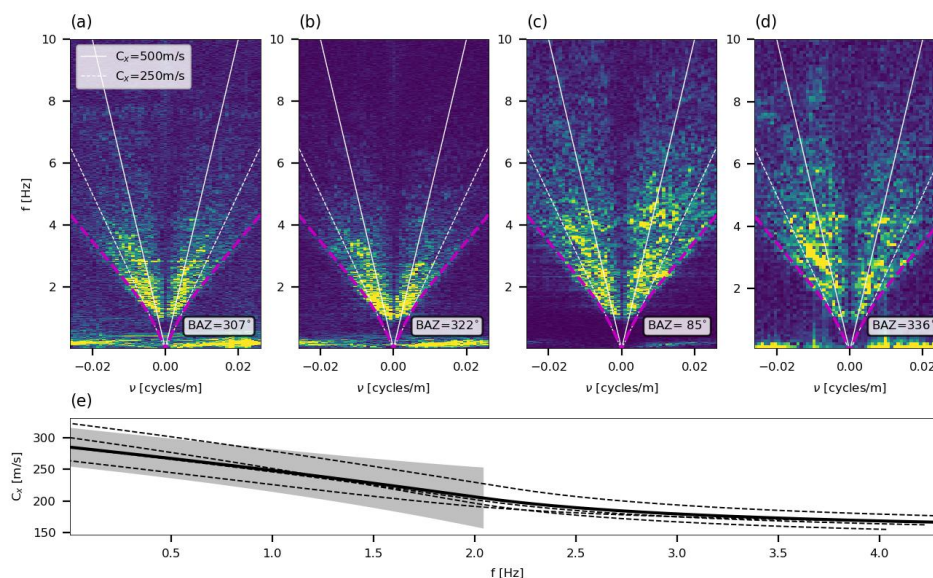350  The observed low apparent velocities, generally symmetric f-k plots,



Figure 5: Panels a-d: Examples of f-k plot for four earthquakes on a segment of the NESTOR cable from 0.35 to 1.5 km. The empirical dispersion curve is indicated in magenta in panels a-d and in panel e. White lines correspond to non-dispersive phase velocities of 500 m/s (solid line) and 250 m/s (dotted line). Panel (e) shows the apparent velocity as a function of frequency obtained for all earthquakes at once (solid black curve) and for each event individually (dashed black curves). Shaded gray area indicates one standard deviation to solid black curve's fit. The dispersion for f > 2 Hz was linearly extrapolated from the fitted curve.

13

351 and similarity between different earthquakes with different back-azimuths
352 (receiver-to-source azimuth), suggest that underwater DAS signals are
353 dominated by Scholte-waves propagating in a broad range of horizontal
354 directions. These dispersive waves are a result of body-wave scattering, and
355 their polarization is radial and vertical, similar to that of Rayleigh waves.
356 Since the analyzed fiber segments are installed on typically flat bathymetry,
357 the radial polarization dominates DAS measurements. Strain-rate
358 measurements of waves propagating at an angle $\theta$ relative to the fiber's axis
359 are modulated by a $cos^2\theta$ (e.g., Kuvshinov et al., 2016; Mateeva et al.,
360 2014), significantly reducing the amplitude of waves closer to normal
361 incidence. Thus, it is expected that the highest amplitude waves recorded by
362 DAS are those traveling along the fiber, with $C_x = C$ (note that generally
363 $C_x \leq C$), i.e., the lowest apparent velocity in the f-k plot (top panels of Figure
364 5). Thus, the phase velocity used for DAS to ground motion conversion is the
365 lowest appartent velocity, represented by the purple curve in Figure *5* which
366 separates the low and high energy regions in the f-k plots. Apparent
367 velocities as a function of frequency, deduced from the curves in Figure *5*,
368 are shown in panel e. The dispersive nature of the waves further supports
369 the conclusion that these are Scholte-waves.

370 Apparent velocities (purple curve in Figure *5*) are obtained for all
371 analyzed events per cable segment. That f-k plots are symmetric and similar
372 for different earthquakes recorded by the same segment suggests similar
373 propagation characteristics, as expected for scattered waves: their
374 propagation and velocity is dictated by local heterogeneities and velocity
375 model. Thus, the same apparent velocity is used for all analyzed earthquakes
376 regardless of source and backazimuth variations. For each event in a specific
377 cable segment, the boundary between the low and high energy regions (top
378 panels of Figure *5*) is determined per frequency by a simple amplitude
379 threshold condition. Then, these $f - \nu$ combinations are averaged per
380 spatial-frequency $\nu$ for all available events, and fitted with a third degree
381 polynomial passing through $f = \nu = 0$. From a certain frequency, this
382 polynomial is linearly extrapolated to obtain the purple curve in Figure *5*.
383 Apparent velocity errors are represented by the gray region in Figure *5*e,
384 indicating one standard deviation for frequencies corresponding to the
385 polynomial fit ($f < 2$ Hz in Figure *5*). For comparison, dispersion curves were
386 obtained independently for each earthquake following the same procedure
387 (dashed curves in Figure *5*e). The standard deviation of the different event
388 specific curves are small: 18.9 and 8.6 m/s at 1 and 4 Hz, respectively,
389 further justifying the use of a single dispersion curve for all earthquakes. For
390 several cable segments, the spatial resolution is inadequate (short cable
391 segments on HCMR and NESTOR, Figures *S4* and *S5*) and f-k plots were fitted
392 with a simpler linear equation passing $f = \nu = 0$, corresponding to non-
393 dispersive waves. In the following section, broadband sensors' acceleration
394 records are converted to strain-rate using the empirical apparent velocities

395 obtained per cable segment. Converted broadband spectra are then
396 compared to DAS spectra.

### 4.3 DAS and broadband comparison

398 Broadband earthquake acceleration spectra are converted to strain-
399 rate and compared with DAS measurements. The conversion was done using
400 the same dispersion curve (Figure *6*) or single apparent velocity (Figure 7) for
401 each cable segment. Here, broadband spectra were corrected for
402 hypocentral distance to match with the different DAS fiber segments. Figures
403 *6* and *7* show DAS strain-rate time series along the cable (left panels), S-
404 wave spectra along the cable (middle panels), and a comparison between
405 DAS and broadband converted strain-rate spectra (right panels) for 4
406 earthquakes recorded on the NESTOR cable. In the right panels, DAS
407 earthquake spectra and mean noise (obtained in section *3*) for each
408 measurement point along the cable segment are plotted as thin black and
409 red curves, respectively, while stacked signal and noise are plotted as thick
410 black and red curves, respectively. These earthquake spectra are resampled
411 in the same manner as noise spectra (McNamara and Buland, 2004) for
412 comparability.

413 Broadband converted acceleration spectra agree with DAS strain-rate
414 spectra when the latter are corrected for site effects. Excellent agreement is
415 observed between DAS and broadband converted spectra for the two closest
416 events in Figure *6* (M2 at 49 km and a depth of 2 km, and M2.6 at 63 km and
417 a depth of 9 km), while the agreement for farther earthquakes is less
418 favorable (M3.3 at 130 km and a depth of 11 km, and M3.6 at 149 km and a
419 depth of 7 km), possibly a result of different propagation effects. In contrast,
420 DAS spectra in Figure *7*, recorded in Methoni bay, are rich in low frequencies
421 and poor in high frequencies. Similar behavior is observed for HCMR, when
422 comparing signals recorded outside (Figures *S5*) and inside (Figures *S6*)
423 Methoni bay, as well as for different MEUST sections (Figures *S7* and *S8*). The
424 amplification observed for MEUST (Figure *S8*) is related to the secondary
425 microseismic peak (Figure *2*), while that observed in Methoni bay is related
426 to the presence of a low velocity (Figure *5* and *S6*) basin, as suggested by
427 the noise peak at 1-2 Hz (Figure *2*). The stronger attenuation inside the basin
428 may be modeled by a decaying exponential term in the form: $exp(-\pi\Delta\kappa f)$
429 (Anderson and Hough, 1984), where $\Delta\kappa$ indicates additional attenuation.
430 Imposing such attenuation on the observed broadband spectra (dashed
431 curves in the right panels of Figure *7*) results in good agreement between
432 high frequency DAS and broadband spectra.

433 To quantify the amplification and attenuation observed by HCMR and
434 NESTOR, the ratio between DAS spectra recorded inside and outside Methoni
435 bay is inspected in Figure *8*. The seemingly tapered edges of these curves
436 represent the signals' amplitudes falling below background noise levels, thus,

437 only frequencies between ~1 and ~15 Hz (depending on SNR) should be
438 considered. Earthquakes recorded inside Methoni bay show significant
439 amplification of up to a factor of 10 at frequencies of 1 to 2 Hz, and stronger
440 attenuation in the 2 to 20 Hz band compared with signals recorded outside
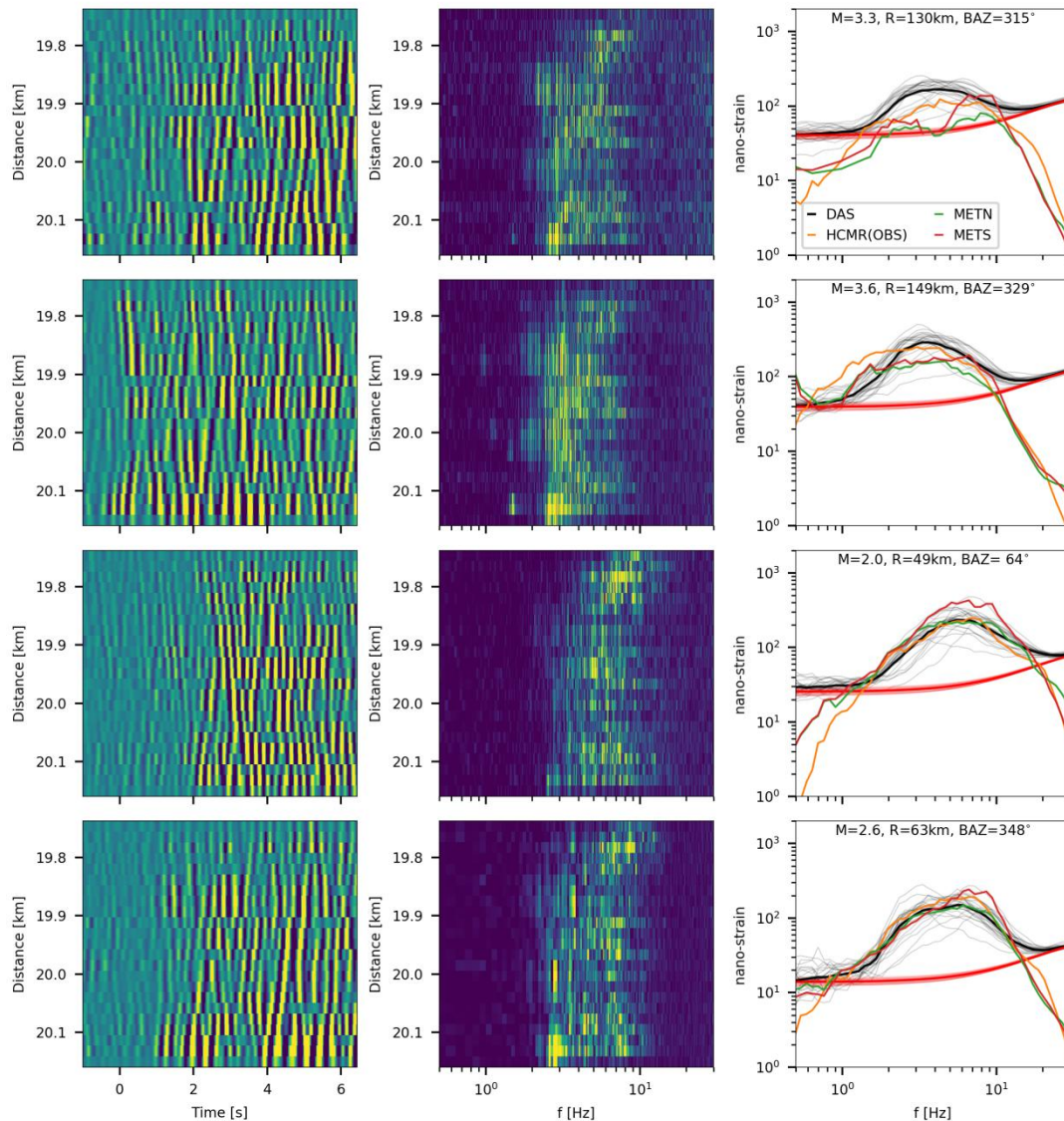441 the bay. This behavior is indicative of sedimentary basins, which are



Figure 6: Spectral analysis for 4 earthquakes recorded by NESTOR between 19.7 and 20.2 km from the interrogator, between 3.1 and 3.3 km depth. Left panels: time series, middle panels: spectra, right panels: strain spectra and converted broadband spectra. Plotted time series (left) were filtered between 1 and 5 Hz. Time in the left panels is relative to the start of the analyzed interval. In the right panels, DAS earthquake and noise spectra for each measurement location along the fiber are indicated by thin black and red curves, respectively, while averages are indicated by thick lines. Green and dark red curves correspond to records from on-land seismometers near the on-land end of the fiber, while the orange curve corresponds to the record of an OBS installed at the end of the HCMR cable.

16

442 generally characterized by low seismic velocities (e.g., Courboulex et al.,
443 2020; Pratt et al., 2003).

444    In the next section, we quantify the ability to detect seismic signals
445 using underwater DAS and compare it to that of broadband seismometers.

## 5 Implications for DAS Detection Capabilities

447    The results presented in the previous section, in particular the
448 conversion between strain and ground motions, based on apparent velocities
449 estimated on each cable segment, are used here to analyze underwater DAS
450 single-channel signal-to-noise ratio (SNR) capabilities, and compare them to
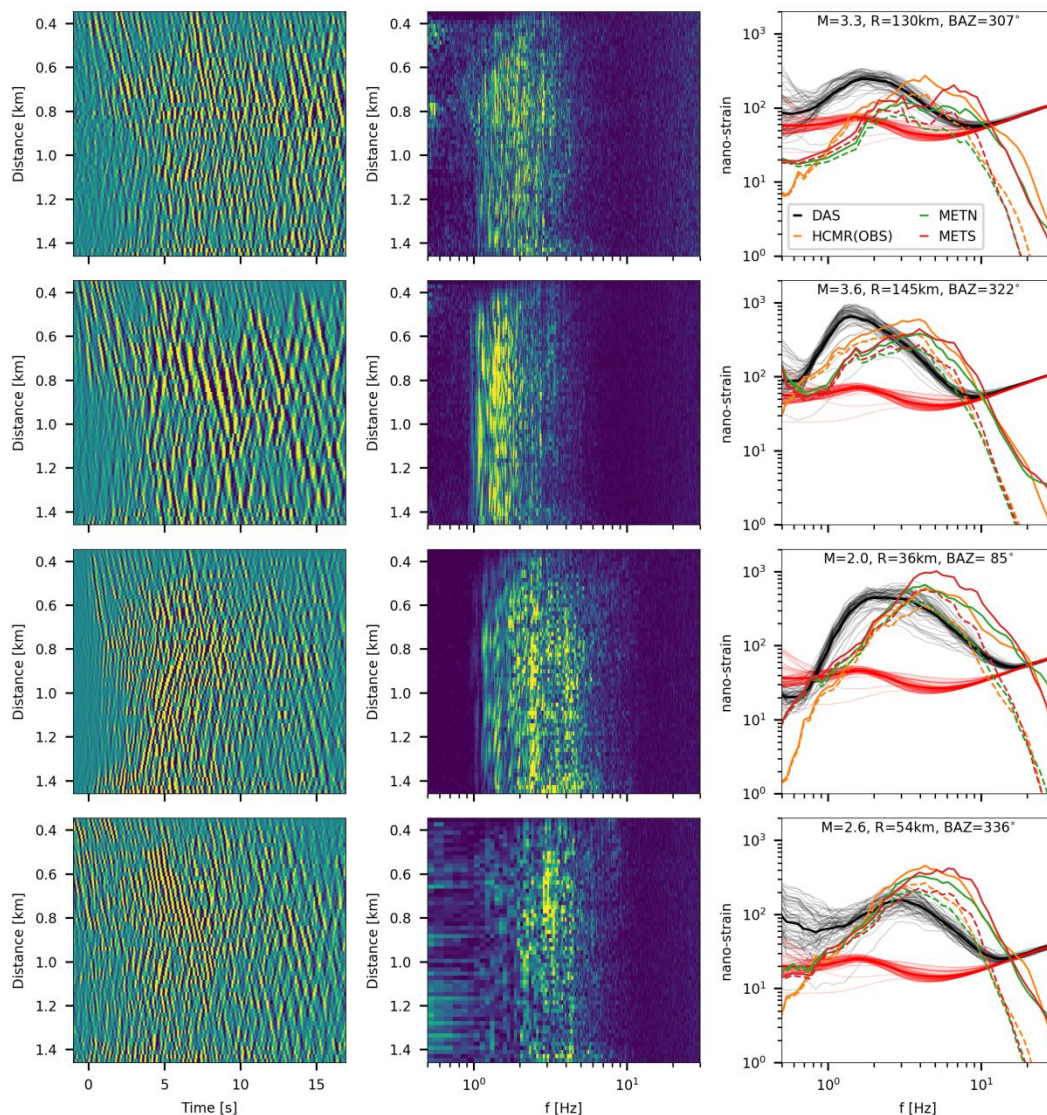


Figure 7: As in figure 6 for a section between 0.35 and 1.5 km from the interrogator, between 3 and 18 m depth. Dashed curves indicate strain-rate converted broadband spectra subject to additional attenuation (Δkappa=0.04 seconds).
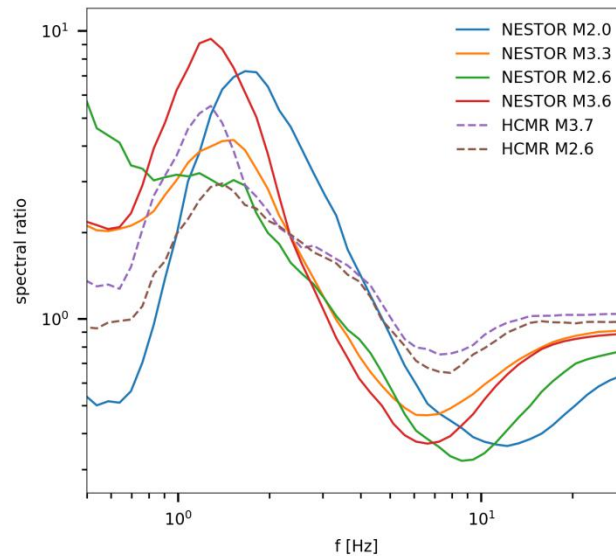
Figure 8: Methoni bay amplification. Spectral ratios of distance corrected DAS spectra for events recorded in and out of Methoni bay: thick black curves in right panels of figure 7 (NESTOR) and S5 (HCMR) divided by thick black curves in right panels of figure 6 (NESTOR) and S4 (HCMR), respectively.

451  those of broadband seismometers. For a valid comparison, this analysis
452  treats DAS signals as independent channels. The spatial coherency between
453  waveforms recorded along the optical fiber, a unique strength of DAS
454  facilitating the implementation of high-performance array detection methods
455  (e.g., Lindsey et al., 2017; Rost and Thomas, 2002), is expected to enhance
456  earthquake detection capabilities, but is not exploited here. In that sense,
457  our analysis is a conservative estimate of the performance of seafloor DAS
458  relative to conventional seismometers. In this section, only the new
459  generation interrogator is considered, since it better represents state-of-the-
460  art DAS capabilities. Because the earthquakes we have recorded are
461  typically observed at $f > 1$ Hz (Figures 5, 6 and 7), this analysis is limited to
462  this frequency band.

463  ## 5.1 S-wave detection on horizontal underwater fibers

464  DAS detection capabilities are analyzed by considering an earthquake
465  model, DAS noise (obtained in section 3), and the apparent velocities
466  (obtained in section 4.2). Earthquake acceleration spectra are simulated
467  using the omega-squared model (Brune, 1970; Madariaga, 1976) describing
468  far field body-wave radiation, and subject to high frequency attenuation
469  (Anderson and Hough, 1984). This model is found to be in good agreement
470  with observed DAS and broadband spectra (not shown). The model, and
471  associated parameter tuning, are described in the supplementary.
472  Horizontally deployed fibers exhibit higher sensitivity to S-waves than P-
473  waves, a function of the phase's polarization with respect to the fiber (e.g.,
474  Kuvshinov, 2016; Mateeva et al., 2014; Papp et al., 2017). Owing to the
475  lower velocities and higher amplitudes of S-waves, they display higher strain

476 amplitudes, compared with P-waves (section 6). Thus, only S-waves are
477 considered in the following analysis. To determine DAS detection thresholds,
478 i.e., signal to noise ratios in a certain frequency-band, for specific cable
479 segments, DAS strain-rate are converted to acceleration noise PSDs
480 (Equation 1) and compared to the earthquake model.

481       Using the apparent velocities for the slow Scholte-waves (e.g., Figure
482 *5*), detection thresholds are found to be similar for DAS and broadband
483 seismometers. Figure *9* shows detection thresholds for MEUST at 12.4 and
484 30.2 km from the interrogator, along with those of adjacent on-land (POSAS)
485 and ocean-bottom (ASEAF) broadband seismometers. Detection thresholds
486 are compared to ground motion accelerations for earthquakes of magnitudes
487 1 and 2 at a hypocentral distance of 50 km. These thresholds indicate great
488 similarity between the detection capabilities of DAS (solid curves in Figure *9*)
489 and nearby broadband OBS (dotted orange curve in Figure *9*) for the same
490 underwater environment and noise conditions (section *3*).

491       The ability to detect a seismic signal using DAS greatly depends on the
492 apparent velocity: at similar acceleration amplitudes, the slower the wave,
493 the higher its strain-rate values (Equation 1). This is illustrated in Figures 10
494 and 11, by modeling DAS and broadband SNR values for different magnitude
495 earthquakes between 1 and 15 Hz. Signals are simulated using the same
496 earthquake model used in Figure 9 at a hypocentral distance of 50 km
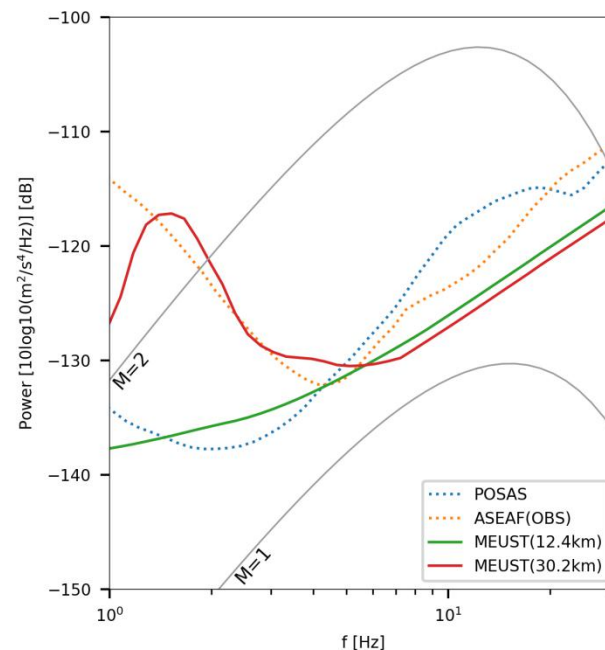


Figure 9: DAS and broadband noise spectra compared to theoretical S-wave spectra. Magnitudes 1 and 2 at distances of 50 km and κ = 0.04 seconds are indicated by solid gray curves. Representative DAS noise curves are shown for MEUST at 12.4 km (solid green) and 30.2 km (solid red). Noise curves for broadband seismic stations on-land POSAS and underwater ASEAF, located near MEUST, are indicated by dotted blue and orange curves, respectively.
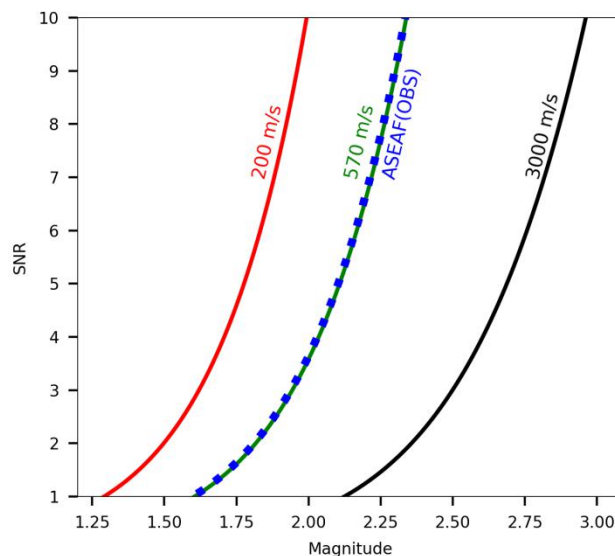
Figure 10: S-wave SNR calculated between 1 and 15 Hz for ground accelerations as a function of magnitude. Earthquake spectra were simulated at a hypocentral distance of 50 km and κ = 0.04 seconds. DAS noise, calculated on MEUST at 12.4 km from the interrogator, was converted to ground accelerations using several non-dispersive apparent velocities. SNR for ASEAF (the OBS at the end of MEUST) are indicated by the dotted blue curve. SNR for DAS with apparent velocities of 200, 570 and 3000 m/s are indicated by solid red, green and black curves, respectively.

497   (Figure 10) and for various distances (Figure 11). Acceleration spectra noise
498   thresholds are obtained for MEUST at 12.4 km from the interrogator using
499   different non-dispersive apparent velocities. The apparent velocity is used to
500   convert DAS strain-rate to acceleration detection threshold, while modeled
501   earthquake acceleration spectra do not account for apparent velocities
502   (supplementary materials). This analysis indicates that for a specific phase
503   velocity, DAS and broadband SNR are equivalent (green and blue curves in
504   Figure 10), while slower and faster waves produce higher and lower SNR on
505   DAS, respectively. In Figure 11, SNR=1 curves are plotted for different
506   magnitude-distance combinations, constituting detection thresholds for
507   various apparent velocities: waves to the right of each curve are detected
508   while those to the left are not. This plot may be used to evaluate the ability
509   to reliably use S-waves for seismic monitoring for different magnitudes and
510   distances.

511        The presented analysis indicates that for a given earthquake, and
512   depending on the ground motion amplitudes, slow phases (e.g., scattered
513   and surface waves) may be detected, while fast phases (e.g., body waves)
514   may not. For instance, plotting DAS earthquake (black) and noise (red)
515   spectra at two different HCMR cable segments (Figure 12), we can observe
516   either low velocity (240 m/s) high energy strain-rate signals (from km 6 to
517   6.3, Figure S5), or high velocity (1690 m/s) low energy strain-rate signals
518   (from km 2.3 to 2.85, Figure S9). Both slow and fast waves are detected for
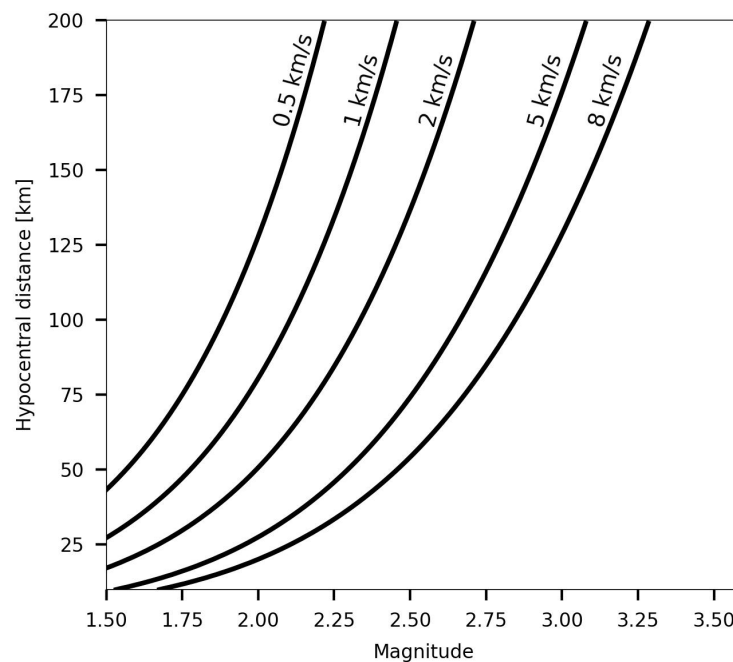519   the M3.7 earthquake (panel a), while only slow waves are detected for the

Figure 11: S-wave detection thresholds (SNR=1), calculated between 1 and 15 Hz, for ground accelerations at different apparent velocities. Earthquake spectra and noise were simulated as in Figure 10 for various magnitudes and hypocentral distances. For each apparent velocity, S-waves at magnitudes-distances to the right of each curve are above noise level.

520    M2.6 earthquake (panel b). Broadband converted strain-rate spectra of the
521    HCMR OBS using the obtained apparent velocities (orange curves) further
522    show that the fast waves of the M2.6 earthquake are below DAS noise levels
523    (dashed orange curve in panel b). Since both analyzed earthquakes display
524    similar    backazimuths    and    distances,    and    thus    similar    propagation
525    characteristics,   the   apparent   velocity   obtained   for   the   M3.7   earthquake
526    (Figure S9) is used to convert the broadband spectra of the M2.6 earthquake
527    to strain-rate (orange dashed curve in Figure 12b).

528        In this analysis, on-land cable segments did not measure any
529    earthquake ground deformations. The longest on-land section is that of
530    MEUST, deployed for 1.6 km: from the interrogator's position to the coast,
531    along a two-lane motorway. This segment displays noise levels similar to
532    those recorded at deeper underwater segments (Figure 3c), and clearly
533    records vehicles driving along the road. That no seismic signals are recorded
534    on this segment is interpreted as a result of high apparent velocities, in
535    agreement with previous studies, which show that on-land Rayleigh waves
536    are faster than ocean-bottom Scholte-waves (e.g., Kruiver et al., 2010; Park
537    et al., 2005). This observation suggests that DAS detection capabilities are
538    enhanced for underwater fibers compared with those installed on-land. Since
539    unlike DAS records, ground motion amplitudes (and thus broadband
540    detection capabilities) are invariant to the wave's velocity, OBS are not
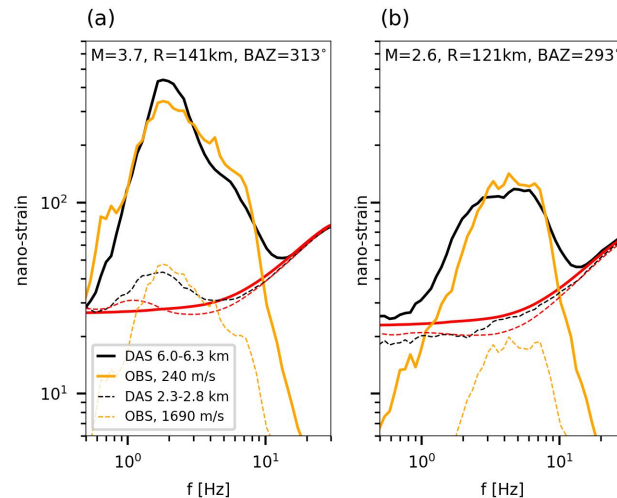541    expected to outperform on-land seismometers.

21

Figure 12: Comparison between earthquakes recorded by two cable segments on HCMR. Thick solid curves and thin dashed curves correspond to stacked DAS spectra (black), stacked DAS noise (red) and broadband converted strain-rate. Broadband spectra was converted to strain-rate using different apparent velocities as noted by the legend. Magnitudes, distances and BAZ values are indicated in the top of each panel.

5.2 P-wave detection on horizontal underwater fibers and implications for earthquake early warning

That fast waves may not be detected by DAS has significant implications for several seismological tasks that rely on the information carried by fast direct body-waves. These objectives include the determination of earthquake location and source parameters, both crucial for seismic monitoring and, in particular, for EEW. Using the P-waves is particularly advantageous for EEW since waiting for the S-waves comes at the cost of delaying alert issuance. However, the detection capabilities of fast, low amplitude, P-waves on horizontal optical fibers is hindered by both the high apparent velocities and near-vertical incident angles; vertically incident P-waves induce transverse deformations on a horizontal cable, while fibers are mostly sensitive to longitudinal deformations. The response of a fiber optic cable to waves propagating at an angle θ with respect to the fiber is modulated by $\cos^2\theta$. Though signals do not vanish completely at θ=90° (Kuvshinov et al., 2016; Mateeva et al., 2014, Papp et al., 2017), they have much smaller amplitude and will hardly be detected.

In practice, P-waves are detected since underwater cables follow the bathymetry and are thus not strictly horizontal (panels c-e of Figure 1), and since incidence angles, especially for scattered P-waves, would typically be smaller than 90°. Even for small magnitudes at large distances, as those analyzed, scattered P-waves are observed for several earthquakes (e.g., in Methoni bay, Figure 4). Thus, for earthquakes relevant for EEW, i.e., medium to big magnitudes at close distances, whose ground motion accelerations are expected to be ~2 orders of magnitude higher than those recorded here

22

567 (e.g., Lior and Ziv, 2020) (Figures 6 and 7). This indicates that underwater
568 telecommunication cables may be reliably used for P-wave detection and
569 thus for EEW, improving alert times for underwater earthquakes. In-depth
570 quantitative analysis of this issue requires further research, beyond the
571 scope of this manuscript, and additional high amplitude earthquake
572 observations.

573       If P-waves cannot be reliably analyzed, the use of S-waves for both
574 tasks is still expected to yield robust estimates, at the cost of time delays.
575 For closely recorded earthquakes, relevant for EEW, these delays are
576 expected to be small, since S-waves follow P-waves by approximately R/8
577 seconds, where R is the hypocentral distance in km (e.g., Lior and Ziv, 2018).

## 6 Conclusions

579       This study presents the most comprehensive analysis to-date of
580 underwater DAS measurements, addressing both noise and earthquake
581 recordings along three underwater dark fibers in the Mediterranean Sea. This
582 analysis presents various noise sources including surface gravity waves,
583 secondary microseisms and local basin resonance. The effect of these noise
584 sources, as well as ocean-bottom – cable coupling, on measured ground
585 deformations is demonstrated using several small (Mw<3.7) well recorded
586 regional earthquakes. Finally, the ability to detect seismic phases using
587 underwater DAS is discusses for both P- and S-waves.

588       A significant correlation is observed between irregular bathymetry and
589 unfavorable DAS measurements (Figures 4, S2 and S3). Flat or smooth
590 bathymetric slopes typically correspond to sediment accumulating regions,
591 while irregular bathymetry prevents sediment deposition. Sedimentary
592 basins are characterized by low seismic velocities (e.g., Figure 5) and
593 excellent coupling (e.g., Figure 4), while regions that lack sedimentary cover
594 are characterized by higher seismic velocities. In addition, deploying
595 underwater fibers over irregular bathymetry may result in uneven coupling
596 and even cable segments hanging in the water column. It is concluded that
597 the bathymetry dictates the measurement quality, by modulating phase
598 velocities and ground-cable coupling.

599       Frequency-wavenumber analysis indicates that underwater DAS
600 earthquake records are dominated by slow scattered dispersive Scholte-
601 waves. Broadband earthquake spectra are converted to strain-rate using
602 apparent velocities obtained via f-k analysis. Since this analysis was done for
603 scattered Scholte-waves, a single apparent velocity or dispersion curve was
604 used for all earthquakes recorded by the same cable segment. However,
605 when analyzing direct phases, apparent velocities will differ depending on
606 the propagation path and wave-fiber incidence angle, requiring an
607 earthquake specific analysis. Excellent agreement is found between DAS and
608 converted broadband spectra, when the latter is corrected for local
609 amplification and attenuation effects. A local sedimentary basin is identified

610 using both coherent noise and earthquake signals, and is shown to amplify
611 and attenuate low and high frequency seismic signals, respectively.

612     Detection capability analysis indicates the great potential of
613 underwater DAS for earthquake detection and monitoring. DAS detection
614 capabilities are found to be strongly correlated with apparent velocities: for
615 the same ground motion amplitudes, slow and fast waves induce high and
616 low energy DAS strain records, respectively. DAS and broadband detection
617 abilities were found to be similar for the recorded earthquake phases (Figure
618 9). That on-land sections did not record the analyzed earthquakes is
619 attributed to higher on-land velocities, a phenomenon that suggests that
620 DAS detection capabilities are enhanced underwater. Our conservative
621 analysis does not use the spatial coherence of DAS data, a powerful property
622 that may be used to denoise coherent signals. Thus, the ability to analyze
623 earthquakes using underwater DAS is expected to be superior to that of
624 broadband sensors, even for equivalent SNR.

625     The results demonstrate the great potential of underwater DAS for
626 seismic monitoring and for providing EEW using standard underwater
627 telecommunication cables. The latter will greatly enhance hazard mitigation
628 capabilities, increase warning times for underwater earthquakes, and
629 potentially save many lives.

## Acknowledgments and Data

## References

645 Allen, R. M., & Melgar, D. (2019). Earthquake Early Warning: Advances, Scientific
646     Challenges, and Societal Needs. *Annual Review of Earth and Planetary Sciences*,
647     *47*(1), 361–388. doi: 10.1146/annurev-earth-053018-060457

648 Aggouras, G., Anassontzis, E., Ball, A. E., Bourlis, G., Chinowsky, W., Fahrun, E.,
649     Grammatikakis, G., Green, C., Grieder, P., Katrivanos, P., Koske, P., Leisos, A.,

650     Ludvig, J., Markopoulos, E., Minkowsky, P., Nygren, D., Papageorgiou, K., Przybylski,

651     G., Resvanis, L. K., & Zhukov, V. A. (2005). Operation and performance of the

652     NESTOR test detector. *Nuclear Instruments and Methods in Physics Research*

653     *Section A: Accelerators, Spectrometers, Detectors and Associated Equipment*, *552*,

654     420–439. doi: 10.1016/j.nima.2005.06.083

655 Anassontzis, E., & Koske, P. (2003). Deep-sea station connected by cable to the shore.

656     *Sea Technology*, *44*, 10–14.

657 Anderson, J. G., & Hough, S. E. (1984). A model for the shape of the fourier amplitude

658     spectrum of acceleration at high frequencies. *Bulletin of the Seismological Society*

659     *of America*, *74*(5), 1969–1993.

660 Brune, J. N. (1970). Tectonic stress and the spectra of seismic shear waves from

661     earthquakes. *Journal of Geophysical Research*, *75*(26), 4997–5009. doi:

662     10.1029/JB075i026p04997

663 Costa, L., Martins, H. F., Martin-Lopez, S., Fernandez-Ruiz, M. R., & Gonzalez-Herraez, M.

664     (2019). Fully Distributed Optical Fiber Strain Sensor With $10^{-12}$ $\epsilon/\sqrt{Hz}$ Sensitivity.

665     *Journal of Lightwave Technology*, *37*(18), 4487–4495. doi:

666     10.1109/JLT.2019.2904560

667 Courboulex, F., Mercerat, E. D., Deschamps, A., Migeon, S., Baques, M., Larroque, C.,

668     Rivet, D., & Hello, Y. (2020). Strong Site Effect Revealed by a New Broadband

669     Seismometer on the Continental Shelf Offshore Nice Airport (Southeastern France).

670     *Pure and Applied Geophysics*. doi: 10.1007/s00024-019-02408-9

671 De Caro, M., Monna, S., Frugoni, F., Beranzoli, L., & Favali, P. (2014). Seafloor Seismic

672     Noise at Central Eastern Mediterranean Sites. *Seismological Research Letters*,

673     *85*(5), 1019–1033. doi: 10.1785/0220130203

674 Fernández-Ruiz, M. R., Soto, M. A., Williams, E. F., Martin-Lopez, S., Zhan, Z., Gonzalez-

675     Herraez, M., & Martins, H. F. (2020). Distributed acoustic sensing for seismic

676     activity monitoring. *APL Photonics*, *5*(3), 030901. doi: 10.1063/1.5139602

677 Finetti, I. (1982). Structure, stratigraphy and evolution of Central Mediterranean.

678     *Bollettino Di Geofisica Teorica Ed Applicata*, *24 (96)*, 247–312.

679 Gabai, H., & Eyal, A. (2016). On the sensitivity of distributed acoustic sensing. *Optics*

680     *Letters*, *41*(24), 5648. doi: 10.1364/OL.41.005648

681     Kruiver, P. P., Deák, A., & Allouche, N. E. (2010). *Extraction of geotechnical properties*
682        *from Scholte waves in underwater environments*. cp-150-00013. doi:
683        10.3997/2214-4609-pdb.150.A05

684     Kuvshinov, B. N. (2016). Interaction of helically wound fibre-optic cables with plane
685        seismic waves: Interaction of fibre-optic cables. *Geophysical Prospecting*, *64*(3),
686        671–688. doi: 10.1111/1365-2478.12303

687     Lamare, P. (2016). The MEUST deep sea infrastructure in the Toulon site. *EPJ Web of*
688        *Conferences*, *116*, 09001. doi: 10.1051/epjconf/201611609001

689     Lindsey, N. J., Dawe, T. C., & Ajo-Franklin, J. B. (2019). Illuminating seafloor faults and
690        ocean dynamics with dark fiber distributed acoustic sensing. *Science*, *366*(6469),
691        1103–1107. doi: 10.1126/science.aay5881

692     Lindsey, N. J., Martin, E. R., Dreger, D. S., Freifeld, B., Cole, S., James, S. R., Biondi, B. L.,
693        & Ajo-Franklin, J. B. (2017). Fiber-Optic Network Observations of Earthquake
694        Wavefields: FIBER-OPTIC EARTHQUAKE OBSERVATIONS. *Geophysical Research*
695        *Letters*, *44*(23), 11,792-11,799. doi: 10.1002/2017GL075722

696     Lior, I., & Ziv, A. (2018). The Relation Between Ground Motion, Earthquake Source
697        Parameters, and Attenuation: Implications for Source Parameter Inversion and
698        Ground Motion Prediction Equations. *Journal of Geophysical Research: Solid Earth*,
699        *123*(7), 5886–5901. doi: 10.1029/2018JB015504

700     Lior, I., & Ziv, A. (2020). Generic Source Parameter Determination and Ground-Motion
701        Prediction for Earthquake Early Warning. *Bulletin of the Seismological Society of*
702        *America*, *110*(1), 345–356. doi: 10.1785/0120190140

703     Longuet-Higgins, M. S. (1950). A Theory of the Origin of Microseisms. *Philosophical*
704        *Transactions of the Royal Society of London. Series A, Mathematical and Physical*
705        *Sciences*, *243*(857), 1–35.

706     Madariaga, R. (1976). Dynamics of an expanding circular fault. *Bulletin of the*
707        *Seismological Society of America*, *66*(3), 639–666.

708     Martins, H. F., Martin-Lopez, S., Corredera, P., Salgado, P., Frazão, O., & González-
709        Herráez, M. (2013). Modulation instability-induced fading in phase-sensitive optical
710        time-domain reflectometry. *Optics Letters*, *38*(6), 872. doi: 10.1364/OL.38.000872

711   Mateeva, A., Lopez, J., Potters, H., Mestayer, J., Cox, B., Kiyashchenko, D., Wills, P.,
712       Grandi, S., Hornman, K., Kuvshinov, B., Berlang, W., Yang, Z., & Detomo, R. (2014).
713       Distributed acoustic sensing for reservoir monitoring with vertical seismic profiling:
714       Distributed acoustic sensing (DAS) for reservoir monitoring with VSP. *Geophysical*
715       *Prospecting*, *62*(4), 679–692. doi: 10.1111/1365-2478.12116

716   McNamara, D. E., & Buland, R. P. (2004). Ambient Noise Levels in the Continental
717       United States. *Bulletin of the Seismological Society of America*, *94*(4), 1517–1527.
718       doi: 10.1785/012003001

719   Papp, B., Donno, D., Martin, J. E., & Hartog, A. H. (2017). A study of the geophysical
720       response of distributed fibre optic acoustic sensors through laboratory-scale
721       experiments: Geophysical response of fibre optic sensors. *Geophysical*
722       *Prospecting*, *65*(5), 1186–1204. doi: 10.1111/1365-2478.12471

723   Park, C. B., Miller, R. D., Xia, J., Ivanov, J., Sonnichsen, G. V., Hunter, J. A., Good, R. L.,
724       Burns, R. A., & Christian, H. (2005). Underwater MASW to evaluate stiffness of
725       water-bottom sediments. *The Leading Edge*, *24*(7), 724–728. doi:
726       10.1190/1.1993267

727   Peterson, J. R. (1993). *Observations and modeling of seismic background noise* (Report
728       No. 93–322; Open-File Report). USGS Publications Warehouse. doi:
729       10.3133/ofr93322

730   Pratt, T. L. (2003). Amplification of Seismic Waves by the Seattle Basin, Washington
731       State. *Bulletin of the Seismological Society of America*, *93*(2), 533–545. doi:
732       10.1785/0120010292

733   R. Fernández-Ruiz, M., Costa, L., & F. Martins, H. (2019). Distributed Acoustic Sensing
734       Using Chirped-Pulse Phase-Sensitive OTDR Technology. *Sensors*, *19*(20), 4368. doi:
735       10.3390/s19204368

736   Rost, S. (2002). Array seismology: Methods and applications. *Reviews of Geophysics*,
737       *40*(3). doi: 10.1029/2000RG000100

738   Sladen, A., Rivet, D., Ampuero, J. P., De Barros, L., Hello, Y., Calbris, G., & Lamare, P.
739       (2019). Distributed sensing of earthquakes and ocean-solid Earth interactions on
740       seafloor telecom cables. *Nature Communications*, *10*(1), 1–8. doi: 10.1038/s41467-
741       019-13793-z

27

742   Vallée, M., Ampuero, J. P., Juhel, K., Bernard, P., Montagner, J.-P., & Barsuglia, M. (2017).

743          Observations and modeling of the elastogravity signals preceding direct seismic

744          waves. *Science*, *358*(6367), 1164–1168. doi: 10.1126/science.aao0746

745   Williams, E. F., Fernández-Ruiz, M. R., Magalhaes, R., Vanthillo, R., Zhan, Z., González-

746          Herráez, M., & Martins, H. F. (2019). Distributed sensing of microseisms and

747          teleseisms with submarine dark fibers. *Nature Communications*, *10*(1), 5778. doi:

748          10.1038/s41467-019-13262-7

749   Zhan, Z. (2020). Distributed Acoustic Sensing Turns Fiber-Optic Cables into Sensitive

750          Seismic Antennas. *Seismological Research Letters*, *91*(1), 1–15. doi:

751          10.1785/0220190112

**Supplementary figure captions**

752 

753 Figure S1: Average PSD sections for MEUST at different frequencies between
754 4 and 9 km from the interrogator.

755 

756 Figure S2: As in figure 4 for a M2 earthquake at approximately 30 km
757 recorded by NESTOR.

758 

759 Figure S3: As in figure 4 for a M2.6 earthquake at approximately 166 km
760 recorded by MEUST.

761 

762 Figure S4: As in figure 5 for 4 earthquakes recorded by NESTOR between
763 19.7 and 20.2 km from the interrogator.

764 

765 Figure S5: As in figures 5 (top) and 6 (bottom) for 2 earthquakes recorded by
766 HCMR between 6 and 6.3 km from the interrogator.

767 

768 Figure S6: As in figures 5 (top) and 6 (bottom) for 2 earthquakes recorded by
769 HCMR between 0.5 and 1.5 km from the interrogator.

770 

771 Figure S7: As in figures 5 (top) and 8 (bottom) for 2 earthquakes recorded by
772 MEUST between 29.7 and 30.7 km from the interrogator.

773 

774 Figure S8: As in figures 5 (top) and 8 (bottom) for 2 earthquakes recorded by
775 MEUST between 12.2 and 12.6 km from the interrogator.

776 

777 Figure S9: As in figures 5 (top) and 8 (bottom) for 2 earthquakes recorded by
778 HCMR between 2.3 and 2.85 km from the interrogator. The earthquake in top
779 panels is detected while that in the bottom panels is not detected.